Journal of Visualization, Vol. 6, No. 4 (2003) 363-370

Numerical and Experimental Investigations on the Mach 2 Pseudo-Shock Wave in a Square Duct

Sun, L. Q.*, Sugiyama, H.*, Mizobata, K.* and Fukuda, K.*

* Department of Mechanical Systems Engineering, Muroran Institute of Technology, 27-1, Mizumoto-cho, Muroran, Hokkaido, 050-8585, Japan.
E-mail: sugiyama@mmm.muroran-it.ac.jp

Received 22 Januany 2003
Revised 26 May 2003

Abstract : This paper describes numerical and experimental investigations for the multiple shock wave/turbulent boundary layer interaction in a Mach 2 supersonic square duct. The numerical simulation is carried out with the Harten–Yee second-order accuracy TVD scheme and the Baldwin–Lomax turbulence model. The flow conditions are a free-stream Mach number of $M_\infty \cong$ 2.0 and a Reynolds number of $Re_\infty = 2.5\times10^7$ and the flow confinements are $\delta_\infty/h = 0.15$ (case A) and $\delta_\infty/h = 0.25$ (case B), respectively. The computational results for both cases show good agreement with the experimental results. Based on these agreements, the flow quantities, which are very difficult to obtain experimentally, are analyzed by numerical simulation. Moreover, the effect of flow confinement on the pseudo-shock wave characteristics is also presented.

Keywords : Pseudo-shock wave, Supersonic flow, Shock wave/turbulent boundary layer interaction, Shock train, CFD, Flow visualization.

1. Introduction

When a supersonic flow is decelerated to subsonic flow in a duct, a complicated multiple shock wave system is produced as the result of shock wave and duct wall turbulent boundary layer interaction. The multiple shock wave system and the resulting mixing region construct a pseudo-shock wave (PSW), which plays a role similar to that of a single normal shock (Matsuo et al., 1999). The PSW significantly affects the performance and efficiency of various flow devices, such as scramjet engine/combustor-isolators, scramjet inlets, supersonic wind tunnel diffusers and supersonic ejectors. Several researchers have investigated the characteristics and structure of the PSW experimentally (e.g., Ikui et al., 1974; Sugiyama et al., 1988, 1998; Carroll and Dutton, 1990) or through numerical simulations (e.g., Hataue, 1989; Carroll et al., 1993; Yamane et al., 1995). However, several important flow quantities of the PSW could not be measured via experimental methods, and numerical simulations have not agreed well with the experimental findings, so that the detailed characteristics, structure, and turbulence phenomena of the PSW have not been fully clarified.

In a previous paper (Sugiyama et al., 2002), by producing a PSW at upstream, mid-stream and downstream locations in a supersonic square duct, the present authors investigated the relationship between the locations and structures of the PSW in a duct by high-speed color schlieren visualization and wall pressure measurements. In the present paper, using numerical simulation, the detailed structure, velocity and pressure distributions of the PSW, which are very difficult to obtain by experimental methods have been investigated. In order to prove the accuracy of the numerical

predictions, the numerical results are compared with the experimental results. The numerical simulation is carried out using the Harten–Yee second-order accuracy TVD scheme (Yee, 1989) and the Baldwin–Lomax algebraic turbulence model.

2. Experimental Apparatus and Method

The experimental apparatus (Sugiyama et al., 2002) is shown in Fig.1. The length and cross section of the test section are 1500 mm and 80×80 mm^2. The test section is connected to the settling chamber via a two-dimension Laval nozzle. The working time of the wind tunnel is 15 s for the Mach 2 condition. The structures of the PSW are visualized via a high-speed color schlieren system, and the light source is a nanospark flash (30 ns). The wall pressures are measured at 43 points along the centerline of the upper wall of the duct using a pressure transducer.

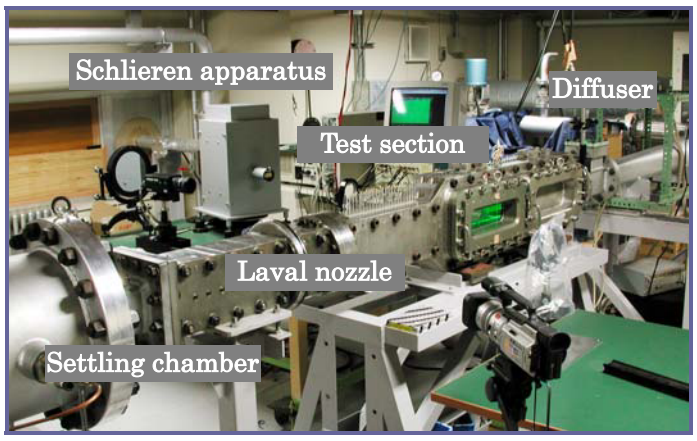

Fig. 1. Experimental apparatus.

3. Numerical Method

3.1 Governing Equations and Turbulence Model

The governing equations are the time-averaged, two-dimensional Navier–Stokes equations, written as follows:

$$\frac{\partial U}{\partial t}+\frac{\partial F}{\partial x}+\frac{\partial G}{\partial y}+\frac{\partial F_{ns}}{\partial x}+\frac{\partial G_{ns}}{\partial y}=0\ , \tag{1}$$

where the vectors U, F, G, F_{ns}, and G_{ns} are given as:

$$U=\begin{bmatrix}\rho\\ m\\ n\\ E\end{bmatrix},\quad F=\begin{bmatrix}m\\ mu+P\\ mv\\ (E+P)u\end{bmatrix},\quad G=\begin{bmatrix}n\\ nu\\ nv+P\\ (E+P)v\end{bmatrix},\quad F_{ns}=\frac{-1}{\mathrm{Re}}\begin{bmatrix}0\\ \tau_{xx}\\ \tau_{xy}\\ u\tau_{xx}+v\tau_{xy}+e_x\end{bmatrix},\quad G_{ns}=\frac{-1}{\mathrm{Re}}\begin{bmatrix}0\\ \tau_{xy}\\ \tau_{yy}\\ u\tau_{xy}+v\tau_{yy}+e_y\end{bmatrix}, \tag{2}$$

with

$$m=\rho u\ ,\quad n=\rho v\ ,\quad \tau_{xy}=u_y+v_x\ ,\quad \tau_{yy}=\frac{4}{3}v_y-\frac{2}{3}u_x\ ,\quad \tau_{xx}=\frac{4}{3}u_x-\frac{2}{3}v_y\ ,$$
$$e_x=\frac{1}{\gamma-1}\left(\frac{\mu_l}{\mathrm{Pr}}+\frac{\mu_t}{\mathrm{Pr}_t}\right)\frac{\partial(c^2)}{\partial x},\quad e_y=\frac{1}{\gamma-1}\left(\frac{\mu_l}{\mathrm{Pr}}+\frac{\mu_t}{\mathrm{Pr}_t}\right)\frac{\partial(c^2)}{\partial y}\ . \tag{3}$$

ρ is the density, E is the energy per unit volume, u and v are the velocity components in x and y directions, respectively, P is the pressure, Re is the Reynolds number, γ (= 1.4) is the ratio of specific heats, μ_l is the laminar viscosity, μ_t is the turbulent viscosity, Pr is the Prandtl number, Pr_t is the turbulent Prandtl number and c is the speed of sound.

The relationship between E and P can be written as

$$P = (\gamma - 1)\left(E - \frac{m^2 + n^2}{2\rho} \right). \tag{4}$$

From the Sutherland viscosity law the laminar viscosity μ_ℓ is obtained. The Baldwin–Lomax algebraic compressible turbulence model is used for the calculation of μ_t. Considering the compressibility, the Van–Driest dumping function is replaced in the turbulence model by

$$D = 1 - \exp[-y^+(\rho/\rho_w)^{1/2}(\mu_w/\mu)/A^+]. \tag{5}$$

The Harten–Yee second-order-accuracy upwind TVD scheme and the central difference are used to solve the convection terms and viscous terms of equation (1), respectively. A second-order-accuracy fractional step procedure is applied in order to obtain a solution for the time term.

3.2 Initial Boundary Conditions and Grid System

The initial condition is given by setting an inviscid normal shock at the rear of the computational region. The inlet condition is uniform across the mainflow, and the boundary layer velocity profile is given by the 1/7-power-law. As the outflow boundary condition, ρ, u, and v are obtained from a one-point extrapolation and the value of P is determined by the experimental result. At the duct centerline, the symmetric quantities are obtained from a second-point extrapolation. Adiabatic, no-slip, solid wall boundary conditions are applied at the wall of the duct. The operating conditions are as follows: free-stream Mach number $M_\infty \cong 2.0$; the flow confinement, i.e., the ratio of the undisturbed boundary layer thickness to the duct half-height, δ_∞/h = 0.15 (case A) and δ_∞/h = 0.25 (case B); Reynolds number $Re_\infty \cong 2.5\times10^7$; stagnation pressure P_0 = 196 [kPa]; stagnation temperature T_0 = 300 [K].

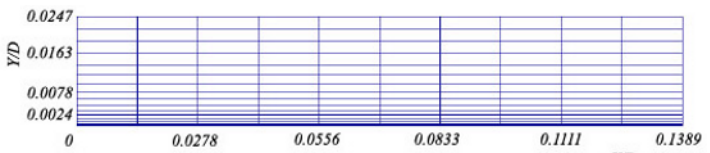

Fig. 2. A part of the meshed computational domain.

A part of the enlarged grid system is shown in Fig.2. The number of mesh points are 1225 (case A) and 865 (case B) in the x direction with equal intervals, and 73 points (both cases) in the y direction with unequal intervals in order to resolve the behavior of the turbulent boundary layer near the wall. The computational region is the central part of the duct with a length of 17 (case A) and 12 (case B) times the height (80 mm). Taking advantage of the symmetry of the flow, only one half of the duct is computed. The grid systems of 1729×73, 865×145 and 1729×145 are used to verify the effect of the mesh size on the numerical results. Although sharper shock waves and finer structures of PSW are captured in the finer grid systems, there are slight differences in the general structures.

4. Results and Discussion

4.1 Structure of the Mach 2 Pseudo-Shock Wave

Figures 3(a) and (b) show the high-speed color schlieren photographs with vertical and horizontal slits for case A. The density contours graph for case A obtained by numerical simulation is shown in Fig.4. The flow is from left to right.

Although, in this experiment, the entire shock train could not be photographed due to the limited field of view of the schlieren apparatus, from Fig.3 we can observe clearly the λ-shaped first shock wave with vertical portion and two bifurcation points, and the second shock wave is concave toward upstream. The boundary layer separates from the wall at the foot of the front leg of the first shock wave. A diamond shaped expansion region exists immediately behind the normal part and rear leg of the first shock. From the numerical simulation results of Fig.4, the structures of the first and second shock waves, the change in the turbulent boundary layer thickness and the flow pattern in the expansion region behind each shock match very well the schlieren photographs. The space between each shock wave and the size of the expansion region behind each shock wave decrease gradually downstream. In addition, the boundary layer gradually thickens downstream.

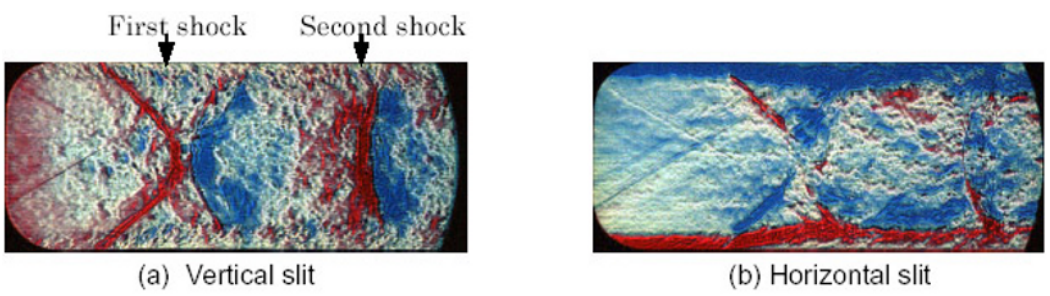

Fig. 3. Schlieren photographs of the Mach 2 pseudo-shock wave taken with vertical and horizontal slit (case A).

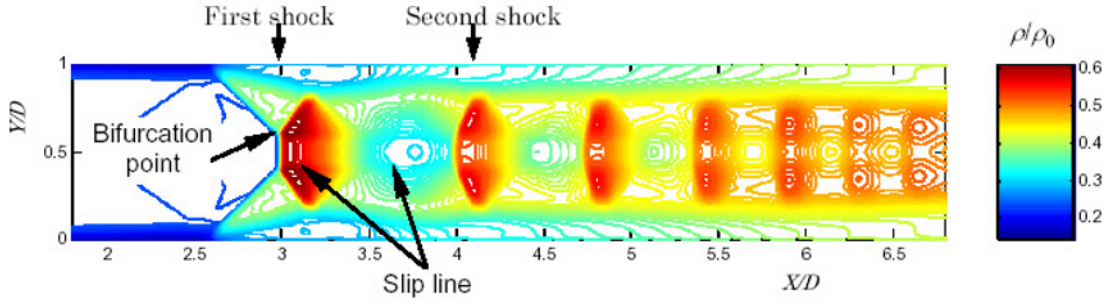

Fig. 4. Density contours (CFD) of the Mach 2 pseudo-shock wave (case A).

4.2 Static Pressure Distributions of the Mach 2 Pseudo-Shock Wave

Figure 5 shows the static pressure distributions along the duct obtained by the present numerical simulation, by experiment and by the Rankine–Hugoniot equation, and the static pressure contours of case A and case B, respectively. The solid black line represents the numerical result and the black circles represent the experimental results of the wall pressure distribution for case A. Similarly, the solid blue line and the blue rectangles represent the numerical and experimental results of the wall pressure distribution for case B. The red and green solid lines represent the numerical results of the static pressure distribution along the centerline of the duct for cases A and B, respectively. The dotted blue line represents the pressure increase induced by an inviscid normal shock of Mach 2. The horizontal axis denotes the distance X from the duct entrance, normalized by the height of the duct D, and the vertical axis represents the static pressure P, normalized by the stagnation pressure P_0 in the upstream settling chamber.

Figure 5 shows that in both cases the wall pressure rise induced by the first shock wave is steep and then continues to rise rather moderately. A slightly jagged wall pressure distribution occurs in case A, and a pressure plateau can be observed between the first and second shock waves,

which cannot be clearly observed in case B. The reason for these behaviors is considered to be that the boundary layer in case A is thinner and the pressure fluctuation induced by each shock in the mainflow can strongly affect the wall pressure. Figure 5 indicates that, in case A, the experimental result of wall pressure is slightly higher than the numerical result. The reason for this may be due to the faulty of the turbulence model used. The computation of case B predicts the magnitude of the wall pressure distribution more precisely. A more thorough numerical investigation is needed for full elucidation of the problem by using other turbulence models or by performing three-dimensional numerical simulations.

The curves of the static pressure distribution along the centerline of the duct in Fig.5 show that the pressure increase due to the first shock is larger and steeper than that due to the successive shocks, but is lower than that of an inviscid normal shock. The strength of each shock in case A is slightly stronger than that in case B. The entire length of the PSW is approximately $X/D \cong 10$ for both cases.

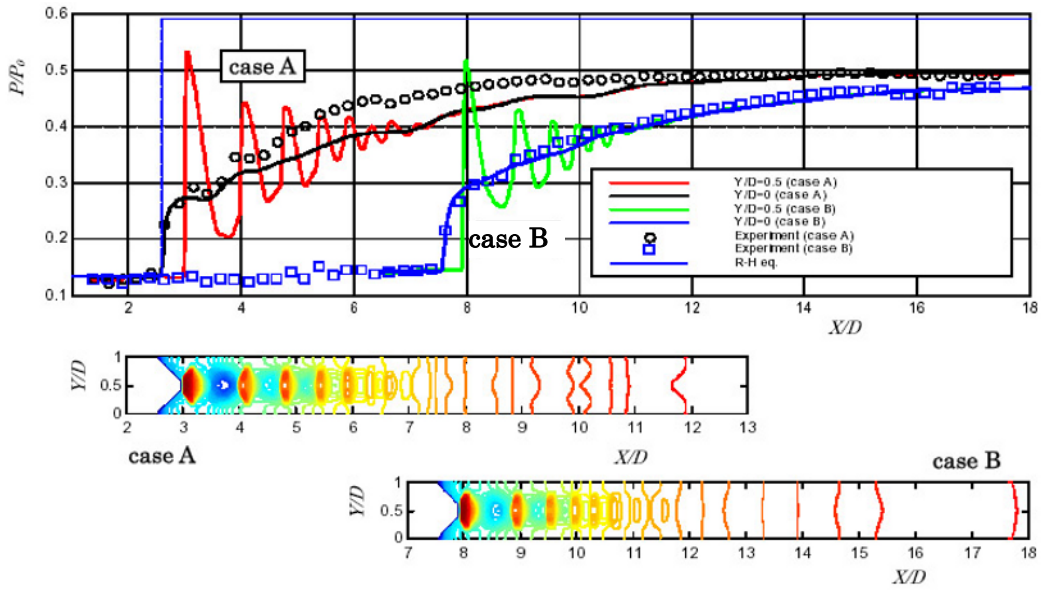

Fig. 5. Static pressure distributions and pressure contours of the Mach 2 pseudo-shock wave.

Figure 6 shows the full details of the static pressure distribution on the central plane of the duct in case A. It is seen that except for the first shock, the static pressure increases saddle shaped, induced by other successive shocks. So the pressure increase induced by the outer portion near the edge of the boundary layer is stronger than that induced by the center portion of the shock. The same tendency is found for case B.

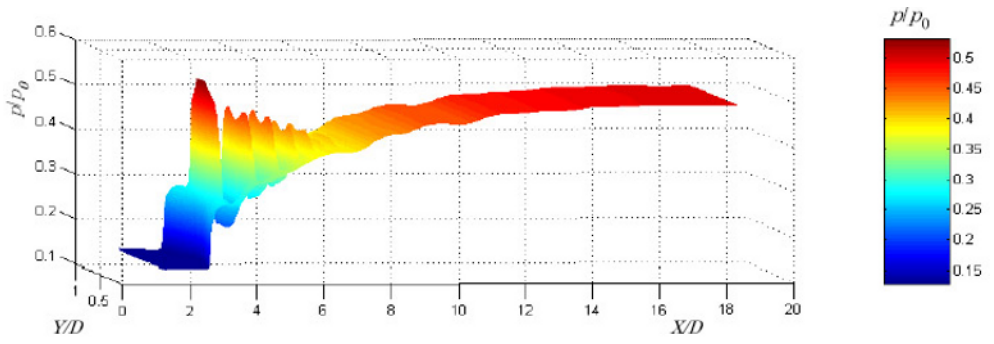

Fig. 6. Static pressure distribution on the central plane of the duct (case A).

4.3 Velocity Distributions of the Mach 2 Pseudo-Shock Wave

Figures 7(a) and (b) show the Mach number contours and the velocity vector distribution, respectively, for case A. Because the deceleration due to the vertical portion of the first shock wave is stronger than that due to the front and rear legs, the weak slip line can be found emanating from the bifurcation point (refer to Fig.4) toward downstream. The flow just outside the boundary layer remains supersonic through the shock train. The core flow behind each shock becomes subsonic and then reaccelerates to supersonic before the next shock appears, and so the velocity profiles at the cross sections are saddle shaped in the shock train region. The flow just behind the shock train is mixed supersonic near the outer edge of the boundary layer (supersonic tongue) and subsonic in the core region. In the mixing region, as the low-speed flow extends to the center of the duct, the entire flow is gradually decelerated to subsonic. Therefore, the velocity profiles changed from trapezoidal behind the shock train to parabolic in the latter half of the mixing region. An increase in the boundary layer thickness is observed passing through the interaction.

The enlarged velocity vector distribution around the first and second shocks of the lower half of the duct is shown in Fig.8, together with the density contours, to indicate the position of the shocks. The blue line in the figure represents the zero-velocity line. The direction of the velocity is changed towards the center by the front leg of the first shock and is changed towards the wall after the rear leg. Similar processes occur after each successive shock, which weaken gradually in the downstream direction. This tendency agrees well with the experimental results reported in previous papers (Sugiyama et al., 1997, 1998) concerning the velocity profile measured via LDV at the Mach 1.83 condition. The boundary layer separates at the foot of the front leg of the first shock. A large reverse flow region can be found under the zero-velocity line near the wall, and a recirculation appears between the rear leg of the first shock and the duct wall. Phenomena similar to those shown in Fig.8 are also observed for case B.

Figure 9 shows the flow Mach number distributions along the duct obtained by numerical simulation. The horizontal axis denotes the normalized distance beginning at the duct entrance, and the vertical axis represents the flow Mach number. The solid red and black lines represent the flow Mach number distributions along the centerline and the line $Y/D = 0.0001$ near the wall of the duct, respectively, for case A. Similarly, the solid green and blue lines represent the flow Mach number distributions in case B. This figure indicates that the flow Mach numbers along the centerline change periodically in an inverse manner to the centerline pressure distributions in Fig.5. The Mach number distributions near the wall indicate that the separation region in case A is slightly larger than that in case B. Therefore, increasing flow confinement reduces the length of the separation region. This agrees with the experimental result reported by Sugiyama (1998). A significant separation region is predicted for both cases. The exact separation length remains speculative. Further experimental and numerical studies are greatly needed in order to solve this ambiguity problem.

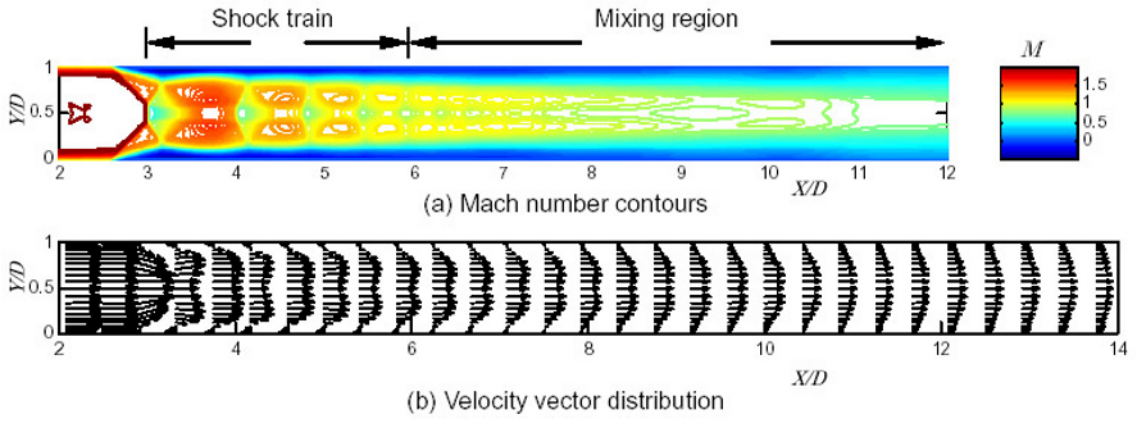

Fig. 7. Mach number contours and velocity vector distribution (case A).

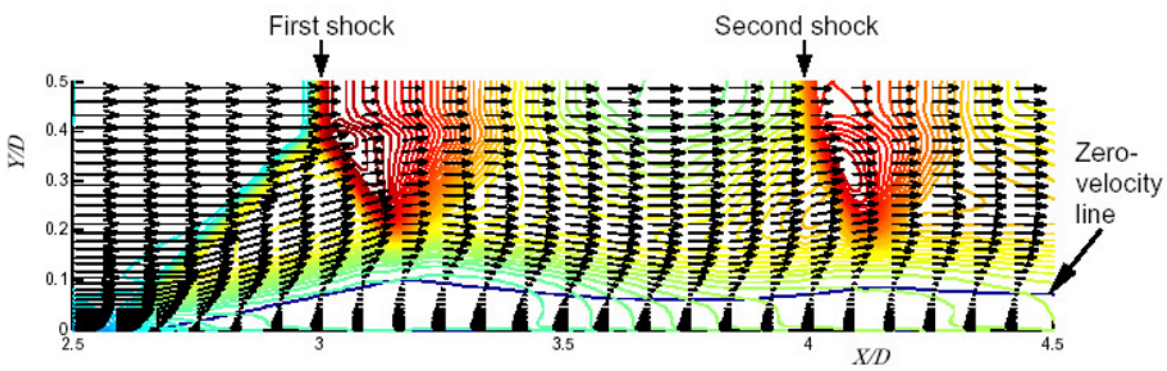

Fig. 8. Detailed velocity distribution around the first and second shock (case A).

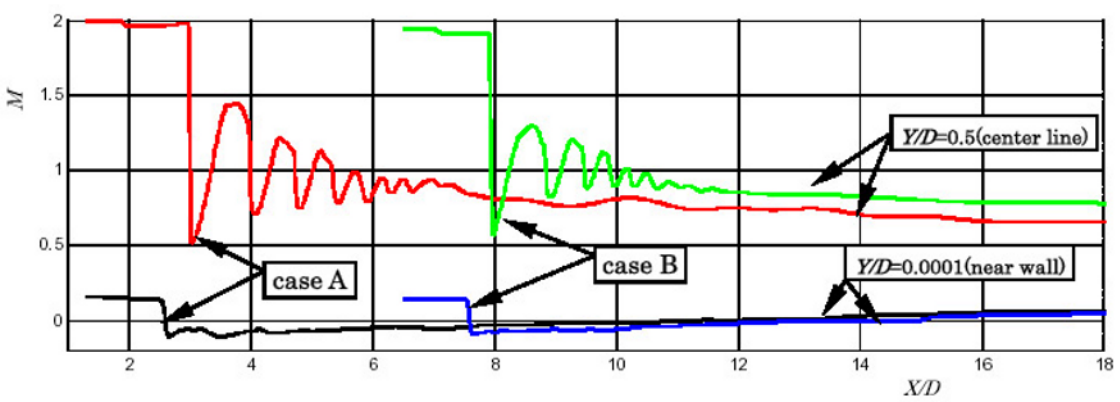

Fig. 9. Mach number distributions along the center line and near the wall of the duct.

5. Conclusion

The numerical simulation and experiments on the Mach 2 PSW in a square duct are performed on the basis of two-dimensional Navier–Stokes equations, using a Baldwin–Lomax turbulence model, and the Mach 2 supersonic wind tunnel. The numerical results agree well with the experimental results. Based on these investigations, the characteristics, structure, pressure and velocity distributions, and the effect of flow confinement on the interaction are analyzed in detail. The primary results are as follows:

1) Through schlieren photographs and density contours obtained experimentally and through numerical simulations, the detailed structures of the Mach 2 PSW are clarified. The first shock wave is λ-shaped, the successive shock waves are concave toward the upstream direction and weaken gradually as they pass downstream. The boundary layer begins to separate at the foot of the front leg of the first shock wave, and the boundary layer thickness increases gradually downstream.
2) The velocity profiles before the shock train are uniformly distributed except in the boundary layer. Because the deceleration of the center portion of each shock is stronger than that of outer portion, the velocity profiles in the shock train became saddle shaped. In the mixing region, because of the mixing effect, the velocity profiles changed from trapezoidal to parabolic in shape.
3) Comparing Mach number distributions, the thinner flow confinement induces a longer separation region length.
4) Because measuring the velocity near the wall is very difficult due to the oscillation of the PSW, the accuracy of the separation region length obtained by numerical simulation cannot be proved

experimentally. More detailed studies, both experimental and computational, should be performed in the future.

References

Matsuo, K., Miyazato, Y. and Kim, H. D., Shock Train and Pseudo-Shock Phenomena in Internal Gas Flows, Progress in Aerospace Sciences 35 (1999), 33-100.

Ikui, T., Matsuo, K. and Nagai, M., The Mechanism of Pseudo-Shock Waves. Bull. JSME, 17-108 (1974), 731-739.

Sugiyama, H., Takeda, H., Zhang, J. P., Okuda, K. and Yamagishi, H., Locations and Oscillation Phenomena of Pseudo-Shock Waves in a Straight Rectangular Duct, JSME International Journal, Series , 31-1 (1988), 9-15.

Sugiyama, H., Arai, T. and Kagawa, K., Multiple Shock Wave/Turbulent Boundary Layer Interactions and Turbulence Phenomena in a Supersonic Rectangular Duct, Proc. of 4th KSME-JSME Fluids Eng. Conf., (1998), 25-28.

Carroll, B. F. and Dutton, J. C., Characteristics of Multiple Shock Wave/Turbulent Boundary-Layer Interactions in Rectangular Ducts, J. of Propulsion and Power, 6-2 (1990), 186-193.

Hataue, I., Computational Study of the Shock-Wave/Boundary-Layer Interaction in a Duct, Fluid Dynamics Research 5 (1989), 217-234.

Carroll, B. F., Lopez-Fernandez, P. A. and Dutton, J. C., Computations and Experiments for a Multiple Normal Shock/ Boundary-Layer Interaction, J. of Propulsion and Power, 9-3 (1993), 405-411.

Yamane, R., Oshima, S., Nakamura, Y., Ishii, T. and Park, M. K., Numerical Simulation of Pseudoshock in Straight Channels, JSME International Journal, Series B, 38-4 (1995), 549-554.

Sugiyama, H., Fukuda, K., Mizobata, K., Endo, K., Sun, L. Q. and Arai, T., Study on Supersonic Internal Flows with Shock Waves (Development of the experimental apparatus for supersonic internal flows and characteristics of the pseudo-shock waves in Mach 2 and 4 internal flows), Trans. JSME (in Japanese), 68-676 (2002), 3295-3301.

Yee, H. C., A Class of High-Resolution Explicit and Implicit Shock-Capturing Methods, NASA TM, 101088, (1989).

Sugiyama, H., Arai, T. and Uno, N., LDV Investigation of Turbulence Phenomena in Multiple Shock Wave/Turbulent Boundary Layer Interactions, Proc. of IUTAM Symp. on Combustion in Supersonic Flows, Champion,M. and Deshaies, B. (eds.), Kluwer Academic Publishers, (1997), 325-332.

Author Profile

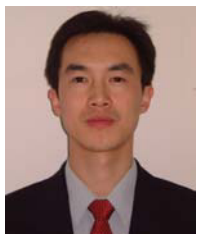

Li Qun Sun: He received his BS degree in 1993 and MS degree in 1999 from Department of Mechanical Engineering, DaLian Railway Institute of Technology (China). He worked in Dalian Railway Institute of Technology for six years. Now he studies for his Ph.D. (Eng) in Muroran Institute of Technology (Japan). His research interests are supersonic flow and CFD, especially supersonic internal flow and shock wave phenomena.

Hiromu Sugiyama: He received his Ph.D. degree in Mechanical Engineering from Tohoku University in 1972. Then he joined a faculty member of Muroran Institute of Technology, and now is a professor. His research interests are high-speed gas flow and multiphase flow phenomena, especially supersonic and hypersonic flow phenomena around next-generation space planes, and shock wave phenomena in dusty gases, bubbly liquids, snows and ices.

Kazuhide Mizobata: He received his Ph.D. degree in aeronautics and astronautics from University of Tokyo. He worked as a research fellow at the National Aerospace Laboratory, Japan, and as a research associate at Tohoku University. He is currently an associate professor at Muroran Institute of Technology. His primary research fields are characterization of supersonic/hypersonic flows and designing of next-generation space transportation systems.

Koichi Fukuda: He received his BS (Eng) degree from Department of Mechanical Engineering, Muroran Institute of Technology. He is a senior researcher in Third Research Center, Technical Research and Development Institute, Japan Defense Agency. Now he studies for his Ph.D. (Eng.) in Muroran Institute of Technology. His research interests are supersonic internal flow, combustion of solid propellant and solid propellant rocket system.